International Journal of Heat and Mass Transfer 51 (2008) 6126–6135

Contents lists available at ScienceDirect

International Journal of Heat and Mass Transfer

journal homepage: www.elsevier.com/locate/ijhmt

Developing slip-flow and heat transfer in trapezoidal microchannels

Hamid Niazmand [a], Metin Renksizbulut [b,*], Ehsan Saeedi [a]

[a] Ferdowsi University of Mashhad, Mechanical Engineering Department, Mashhad, Iran
[b] University of Waterloo, Mechanical and Mechatronics Engineering Department, Waterloo, Ontario, Canada N2L 3G1

ARTICLE INFO

Article history:
Received 2 August 2007
Received in revised form 3 April 2008
Available online 12 June 2008

Keywords:
Slip-flow
Rarefaction
Temperature-jump
Trapezoidal microchannel
Entrance region
Friction coefficient
Heat transfer coefficient

ABSTRACT

Simultaneously developing velocity and temperature fields in the slip-flow regime are investigated numerically in trapezoidal microchannels with constant wall temperatures. A wide range of channel aspect ratios ($0.25 \leqslant \alpha \leqslant 2$) and side angles ($30^\circ \leqslant \phi \leqslant 90^\circ$) are considered in the Reynolds number range $0.1 \leqslant Re \leqslant 10$. A control-volume based numerical method is used to solve the Navier–Stokes and energy equations with velocity-slip and temperature-jump at the walls. As characterized by the Knudsen number ($Kn \leqslant 0.1$), the effects of rarefaction on the key flow features are examined in detail. Major reductions in the friction and heat transfer coefficients are observed in the entrance region due to large amounts of velocity-slip and temperature-jump. In the fully developed region, the friction coefficient decreases strongly both with increasing *Kn* and aspect ratio but has a weaker dependence on the side angle. The heat transfer coefficient also decreases strongly with increasing rarefaction and aspect ratio; however, as the aspect ratio increases, its sensitivity to *Kn* decreases. Practical engineering correlations are also provided for fully developed flow friction and heat transfer coefficients.

1. Introduction

In recent years, advances in manufacturing technologies and striking developments in micro-fluidic devices have renewed interest in laminar flows through microchannels with irregular cross-sections. Gas flow in a micron-size channel is associated with some degree of non-continuum effect, which is characterized by the Knudsen number, *Kn*, defined as the ratio of the mean-free-path to the appropriate macroscopic flow scale. For the slip-flow regime, which is commonly encountered in microchannel flows, *Kn* is in the range $10^{-3} \leqslant Kn \leqslant 10^{-1}$ and slight rarefaction effects occur adjacent to the walls. In order to account for these rarefaction effects, slip/jump conditions are taken to exist across a thin Knudsen layer, which extends approximately one mean-free-path from the walls. Experimental observations indicate that beyond this layer the continuum hypothesis is valid. Therefore, in the slip-flow regime, it is common practice to use the standard Navier–Stokes and energy equations with only the boundary conditions modified for velocity-slip and temperature-jump at the walls.

For shorter channels, the entrance region is of much importance, where the velocity and temperature fields undergo major transformations from essentially uniform inlet profiles to fully developed profiles. In the entrance region, an analytical solution of the problem is not feasible due to the non-linear inertia terms in the momentum equations. However, the classical boundary-layer approximations provide major simplifications and a number of semi-analytical solutions have been obtained for laminar slip-flow development in the entrance region of circular and parallel-plate channels [1,2]. Clearly, boundary-layer approximations are not suitable for microchannel flows, which are characterized by very low Reynolds numbers.

Gas flows in microchannels have received considerable attention and have been experimentally, numerically and analytically studied by many researchers (e.g. [3–9]). Most of the numerical simulations and analytical solutions were performed in 2D with simplifications in the governing equations. A survey of the available literature on low Mach number flows indicates rather limited information on 3D flows in the slip-flow regime, such as in the entrance region of microchannels. Heat transfer in microchannels has also been studied by a number of researchers mainly in the context of fully developed slip-flows in simpler geometries, which have been recently reviewed [10], and therefore, will not be repeated here. Most of the previous studies as well as the present work consider channels with constant wall temperatures; however, fully developed flows in channels subjected to uniform wall heat fluxes have also been studied (e.g., [11]).

In the literature, studies on thermally developing micro flows are limited to the application of fully developed analytical velocity profiles in the solution of the energy equation for circular tubes and rectangular microchannels. Larrodé et al. [12] obtained an analytical solution for developing heat transfer in a constant wall temperature circular tube, where a fully developed slip velocity profile was employed. The temperature-jump condition was applied at

* Corresponding author. Tel.: +1 519 884 9674x33977; fax: +1 519 885 5862.
E-mail address: metin@uwaterloo.ca (M. Renksizbulut).

0017-9310/$ - see front matter © 2008 Elsevier Ltd. All rights reserved.
doi:10.1016/j.ijheatmasstransfer.2008.04.007

Nomenclature

A_c	cross-sectional area
$2a$	top side of the channel (Fig. 1)
c_p	specific heat at constant pressure
D_h	hydraulic diameter, $4A_c/P_{wet}$
f	friction coefficient, $\tau_w/\left(\rho W_i^2/2\right)$
H	channel height
h	heat transfer coefficient
Kn	Knudsen number, λ/D_h
k	thermal conductivity
Nu	Nusselt number, hD_h/k
P_{wet}	wetted perimeter
Pe	Peclet number, $RePr$
Po	Poiseuille number, fRe
Pr	Prandtl number, $c_p\mu/k$
p	pressure
Re	Reynolds number, $\rho W_i D_h/\mu$
T	temperature
u, v, w	velocity components in the x, y, z-directions
$\vec{V}$	velocity vector
W_i	uniform axial inlet velocity
z^+	nondimensional axial position, $z/(D_hRe)$
z^*	reciprocal Graetz number, $z/(D_hRePr)$

Greek symbols

α	aspect ratio, $H/(2a)$
γ	specific heat ratio, c_p/c_v
λ	molecular mean-free-path
μ	dynamic viscosity
ρ	density
τ_w	wall shear stress
ϕ	acute side-angle (Fig. 1)

Subscripts

fd	fully developed
i	inlet
m	mean
S	slip condition
w	wall

the wall in the slip-flow regime. Yu and Ameel [13,14] presented an analytical treatment of the slip-flow problem for rectangular microchannels. Developing and fully developed Nusselt numbers were obtained for hydrodynamically fully developed slip-flow. Note that, in these studies, the effects of axial heat conduction, which becomes important for low Reynolds number conditions, were neglected. Similarly, Lee and Garimella [15] solved the energy equation with a specified velocity profile to study heat transfer in the entrance region of rectangular microchannels subject to uniform wall temperature and uniform wall heat flux boundary conditions. Axial conduction was assumed negligible; moreover, the slip effect was also neglected in the prescribed fully developed velocity profile. Local and average Nusselt numbers were presented for a wide rage of aspect ratios.

Zhen et al. [16] performed a direct Monte Carlo simulation for heat transfer calculations of low speed short microchannel flows. Straight rectangular channels with various aspect ratios were considered. It was concluded that the 2D simplification for a 3D rectangular microchannel flow seems to be reasonable only for aspect ratios smaller than 0.2. Hong and Asako [17] studied the heat transfer characteristics of two dimensional compressible gaseous flows in microchannels and microtubes. Constant wall temperature was considered and a correlation for the prediction of the heat transfer rates was proposed. Important issues associated with microchannel heat transfer were reviewed by Hetsroni et al. [18] including viscous dissipation and axial heat conduction in the fluid as well as channel walls under constant heat flux condition. Maranzana et al. [19] have also investigated the effect of axial conduction in the wall on the heat transfer in microchannels. An axial conduction number defined as the ratio of conductive to convective heat flux was introduced and conditions under which axial conduction is considerable were identified.

Renksizbulut et al. [10] conducted a numerical study of simultaneously developing slip-flow and heat transfer in rectangular microchannels for a wide range of aspect ratios and Knudsen numbers. It was found that the heat transfer and friction coefficients are finite at the channel inlet and greatly reduced in the entrance region due to velocity-slip and temperature-jump at the walls. Poiseuille and Nusselt number correlations were also provided for fully developed friction and heat transfer coefficients, including the effects of axial heat conduction.

The above literature survey indicates a state of incomplete information for simultaneously developing slip-flow and heat transfer in trapezoidal microchannels. In the present work, a wide range of channel aspect ratios ($0.25 \leqslant \alpha \leqslant 2$) and acute side angles ($\phi = 30°, 45°, 60°, 90°$) are considered for $Kn \leqslant 0.1$ in the range $0.1 \leqslant Re \leqslant 10$ with $Pr = 1$. Three-dimensional Navier–Stokes and energy equations with velocity-slip and temperature-jump boundary conditions have been solved numerically by a control-volume method. In particular, the entrance region has been fully investigated, where the major fractions of pressure drop and heat transfer occur in shorter channels that are frequently encountered in modern compact heat exchangers as well as in various types of microfluidic devices found in MEMS.

2. Formulation

Fig. 1 shows the basic geometric variables that describe a trapezoidal channel along with the adopted coordinate system. The top wall of the channel ($2a$) is held constant and the channel height (H) is calculated from the specified aspect ratio defined as $\alpha = H/(2a)$. Thus, a unique cross-section is obtained for a given α and acute side angle ϕ. The channel length is set to a value larger than the estimated hydrodynamic entrance length of the flow to ensure that fully developed conditions are achieved at the exit. Since the entrance length is a function of Re, Kn and geometry, the channel length has been adjusted according to the case under consideration.

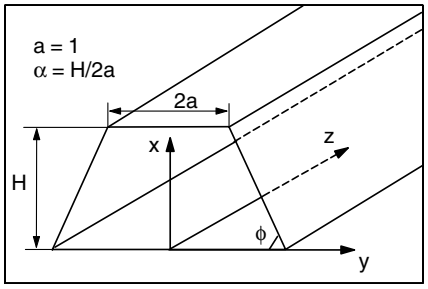

Fig. 1. Channel geometry and the coordinate system.

The governing equations of mass, momentum and energy conservation for the constant-property laminar flows under study are:

$$\vec{\nabla}\cdot\vec{V}=0 \tag{1}$$

$$\rho\frac{\mathrm{D}\vec{V}}{\mathrm{D}t}=-\nabla p+\mu\nabla^2\vec{V} \tag{2}$$

$$\rho c_p\frac{\mathrm{D}T}{\mathrm{D}t}=k\nabla^2 T \tag{3}$$

Body forces and viscous dissipation are ignored in the present work. Inflow boundary conditions correspond to a uniform inlet temperature $T = T_i$ and a flat velocity profile such that $u = v = 0$ and $w = W_i$. For outflow, zero-gradients along the axial flow direction are applied to all variables: $\partial f/\partial z = 0$, where $f = u, v, w, T$. The pressure is set to zero at the outlet, while zero gradients are assigned to all other boundaries including the inlet considering the fact that the inlet velocity is specified. At the symmetry plane ($y = 0$), the normal velocity component as well as the normal gradients of all other flow variables are set equal to zero, indicating no advection or diffusion across this plane. The temperature of the channel walls T_w is specified to be axially and peripherally uniform and higher than the inlet stream temperature T_i. Furthermore, the flow satisfies the velocity-slip and temperature-jump conditions at the walls. The first order velocity-slip condition for an ideal gas is given by [20]:

$$w_s - w_w = \lambda\left(\frac{2-\sigma_v}{\sigma_v}\right)\left(\frac{\partial w}{\partial n}\right)_w \tag{4}$$

Other velocity components are specified similarly. Here, the subscript w identifies a wall with a normal coordinate n. Likewise, the first order temperature-jump condition at the wall is:

$$T_s - T_w = \left(\frac{2-\sigma_T}{\sigma_T}\right)\left(\frac{2\gamma}{\gamma+1}\right)\left(\frac{\lambda}{Pr}\right)\left(\frac{\partial T}{\partial n}\right)_w \tag{5}$$

The parameters σ_v and σ_T in Eqs. (4) and (5) are the tangential-momentum and energy accommodation coefficients, respectively, which are taken as unity in the present study. A specific heat ratio of $\gamma = 1.4$ is used in all computations.

The Reynolds number, $Re = \rho W_i D_h/\mu$, is based on the uniform inlet velocity and the hydraulic diameter D_h. The density is constant, and therefore, the mean axial velocity W_m is equal to the uniform inlet velocity W_i everywhere in the channel. The Knudsen number is based on the hydraulic diameter and defined as $Kn = \lambda/D_h$. The Prandtl number is set equal to 1, while the Reynolds number is specified in the range $0.1 \leqslant Re \leqslant 10$. It is well known that gas compressibility effects can be neglected only at relatively low Mach numbers, Ma. From the definitions of Re, Kn and Ma, it follows that:

$$Re = \frac{Ma}{Kn}\sqrt{\frac{\pi\gamma}{2}} \tag{6}$$

Hence, except for Knudsen numbers in the upper end of the slip-flow regime, gas flows in microchannels can be considered incompressible for a wide range of Reynolds numbers.

3. The numerical method and validation

The governing equations are integrated over the corresponding control volumes upon transformation into a generalized non-orthogonal coordinate system. The principle of the numerical method is based upon the calculation of the velocity field from momentum equations using an existing or approximate pressure field. This velocity field does not necessarily satisfy the mass conservation equation, and thus a velocity correction is introduced. A velocity potential is assigned to the velocity correction according to the Hodge decomposition theorem, which states that any vector function can be decomposed into a divergence-free component and the gradient of a scalar potential. This is consistent with the fact that an intermediate velocity field obtained form the momentum equations using an existing pressure field carries the exact vorticity information, and therefore, the velocity correction comes from an irrotational field that can be described with a velocity potential. The continuity equation is then transformed into a Poisson equation for the velocity potential, which is solved with a matrix-free and pre-conditioned version of GMRES (Wigton et al. [21]). This method is capable of enhancing the convergence rate of the Poisson solver as compared to the traditional successive-over-relaxation solvers. Finally, the pressure correction is directly related to the velocity correction through the momentum equations. This numerical scheme was originally developed by Chorin [22], and improved further by Dwyer [23] and the present authors [24] for internal flows.

A systematic refinement study was performed to determine the appropriate spatial discretization for grid independent numerical results. The grid points are clustered near the channel walls and in the entrance region where large gradients exist. The quantities examined for the grid independence study were the key flow parameters and it was found that a mesh size of 50×50 provides satisfactory cross-sectional resolution. Also, the effect of axial grid resolution on the numerical results indicated variations of less than one percent in all monitored parameters for a mesh size containing more than 150 grid points in the axial direction. Therefore, a minimum mesh size of $50 \times 50 \times 150$ was used with grid expansion ratios of about 1.07 and 1.06 in the x- and z-directions, respectively. However in the y-direction, a variable expansion factor has been used for each specified side angle ϕ in order to cluster the grid points into the acute corner region. Extensive numerical validation studies have been conducted for flows in pipes, rectangular and trapezoidal ducts, and between parallel plates, which can be found in Renksizbulut et al. [10,24], and therefore, will not be repeated here. Pressure distributions, velocity profiles, friction factors and heat transfer coefficients were all compared with available experimental and analytical results from the literature.

4. Results and discussion

4.1. The flow field

In incompressible flow through a channel (with or without slip), non-axial velocity components are zero and pressure is uniform

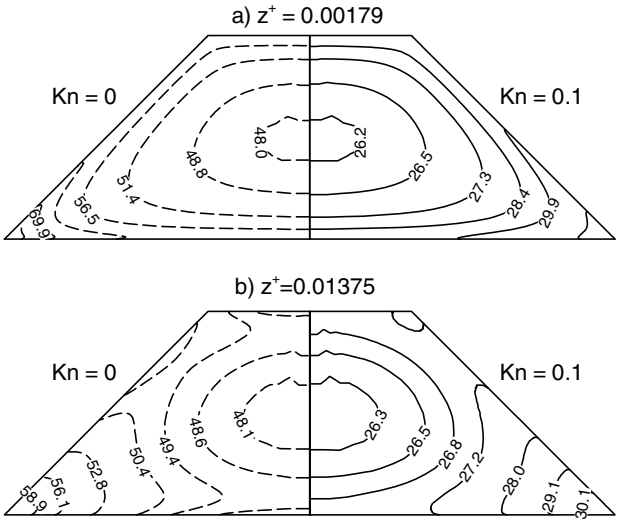

Fig. 2. Cross-sectional pressure distributions at $Re = 10$, $\phi = 45°$, and $\alpha = 1$: dashed lines $Kn = 0$, solid lines $Kn = 0.1$; (a) $z^+ = 0.00179$ and (b) $z^+ = 0.01375$.

over a given cross-section only in the fully developed region. In the entrance region, the flow is three dimensional with non-uniform pressure fields at each location. Cross-sectional pressure distributions at two axial planes close to the inlet are shown in Fig. 2. The flow is at $Re = 10$ in a trapezoidal channel with a side angle of $\phi = 45^\circ$ and an aspect ratio of $\alpha = 1$. The nondimensional axial length is defined as $z^+ = z/(D_h Re)$, and $\rho W_i^2/2$ is used to normalize pressure. In each cross-section, the dashed lines refer to no-slip conditions, while the slip-flow case at $Kn = 0.1$ is indicated by solid lines. In the former case, due to complete fluid stagnation at the walls, the maximum pressures are found near the walls and particularly in the corner regions. In the latter case, velocity-slip leads to significant reductions in the pressure gradients at the same location as clearly seen in Fig. 2a. Farther down stream from the inlet in Fig. 2b, similar pressure variations are also present, however to a lower extent. These high pressures near the walls and specifically in the corner regions direct the fluid towards the channel core as well as in the axial direction, which lead to the development of velocity overshoots near the walls and in the acute corners. This is clearly seen in Fig. 3, which shows the corresponding three dimensional velocity profiles. The axial locations (a) $z^+ = 0.00179$ and (b) $z^+ = 0.01375$ are in the developing flow region, while the flow is fully developed at (c) $z^+ = 0.4055$ where the pressure is uniform over the cross-section and the flow attains its maximum velocity in the channel core. The cross-sectional maximum velocity and its location in the fully developed region compare well with available data [25] for all cases considered here.

Allowing for slip at the walls reduces the amount of cross-sectional and axial pressure gradients, and as a result, the velocity overshoots largely vanish as seen in Fig. 4. This figure shows the velocity profiles for $Kn = 0.1$ at the same axial locations as in Fig. 3. The prescribed uniform inlet velocity profile is only slightly affected at the first axial location (Fig. 4a) due to very large veloc-

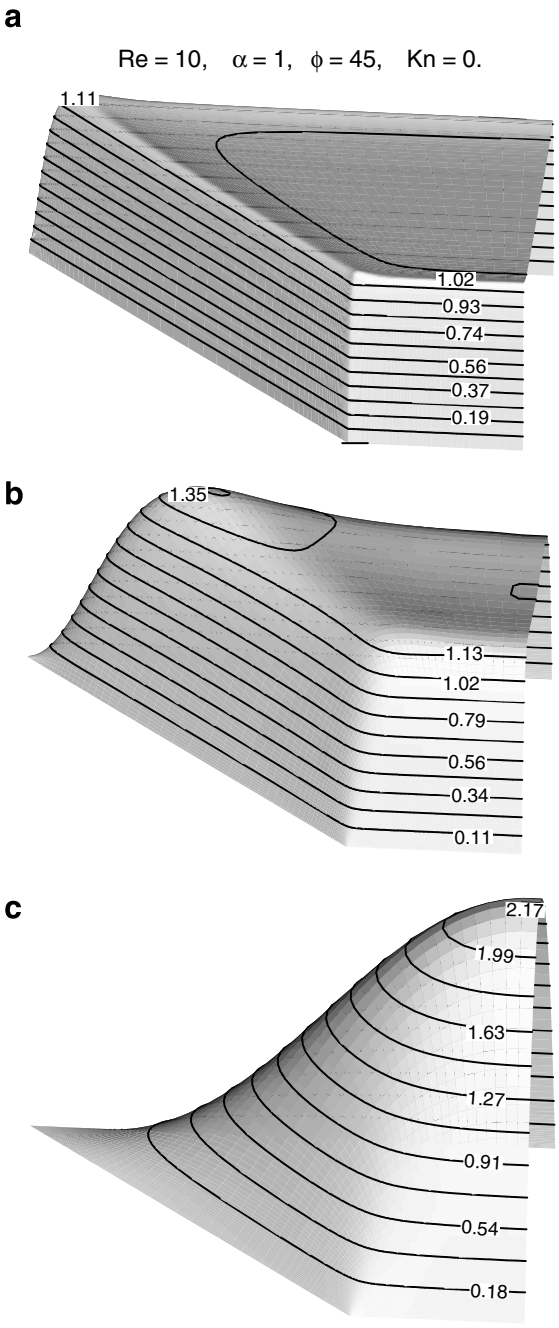

Fig. 3. Velocity profiles in a trapezoidal channel with $\phi = 45^\circ$, and $\alpha = 1$ at $Re = 10$ for $Kn = 0$: (a) $z^+ = 0.00179$, (b) $z^+ = 0.01375$ and (c) $z^+ = 0.40551$.

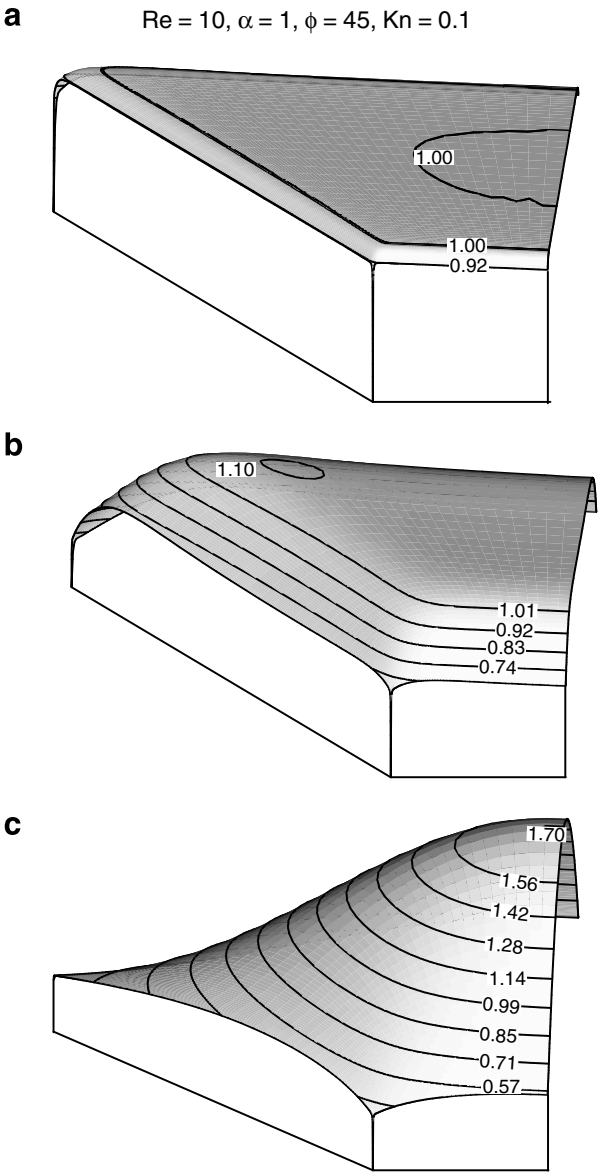

Fig. 4. Velocity profiles in a trapezoidal channel with $\phi = 45^\circ$, and $\alpha = 1$ at $Re = 10$ for $Kn = 0.1$: (a) $z^+ = 0.00179$, (b) $z^+ = 0.01375$ and (c) $z^+ = 0.40551$.

ity-slip near the entrance. High velocity-slip is directly related to both the high Knudsen number and the large normal velocity gradients in this region. Yet, slight velocity overshoots can still be observed in the axial location $z^+ = 0.01375$ in Fig. 4b corresponding to higher pressure gradients in the corner region (see Fig. 2b).

In general, corners are regions of low velocity-slip due to weaker velocity gradients. The amount of velocity-slip at a given *Kn* decreases as the flow approaches a fully developed state. This is illustrated in Fig. 5 where the axial variation of peripherally averaged slip velocity is plotted for several Knudsen numbers for a channel with $\phi = 45°$ and $\alpha = 1$ at $Re = 1$. The constant values of velocity-slip in the fully developed region also serve as a good indicator of the entrance length. Interestingly, this figure shows that the entrance length is only marginally influenced by increasing Knudsen number, which may appear counterintuitive. In slip-flow, momentum diffusion towards the channel core is slower due to weaker transverse velocity gradients, which would normally lead to longer entrance lengths with increasing *Kn*. However, as compared to a no-slip flow, the final fully developed velocity profile in slip-flow is relatively flatter, and therefore, closer to the inlet profile, hence requiring less axial distance to develop. These opposing effects largely cancel each other, making the entrance length a very weak function of *Kn*. Channels with other aspect ratios and side angles display similar behavior.

In Fig. 6, the axial variation of the friction coefficient or the Poiseuille number ($f_{app}Re$) is shown as a function of Knudsen number for a trapezoidal channel with $\phi = 45°$ and $\alpha = 1$ at $Re = 1$. The nondimensional pressure drop along the channel expressed in the form of an apparent Fanning friction factor is defined as [25]:

$$\frac{\Delta\bar{p}}{\rho W_i^2/2} = \frac{4z}{D_h} f_{app} = 4z^+ f_{app} Re \tag{7}$$

where $\bar{p}$ is the local average pressure and $\Delta\bar{p} = p_i - \bar{p}$ represents the pressure drop from the channel inlet. There are two contributions to pressure drop in the flow development region: the wall shear and the change in momentum flow rate. The change in momentum flow rate is due to the evolution of the velocity profile from a flat inlet profile to a fully developed profile along the channel. When the no-slip boundary condition is applied, a major part of the pressure drop in the entrance region is basically used up for velocity profile development. In slip-flow, both contributors to the pressure drop are greatly influenced. The amount of pressure drop required for velocity profile development decreases significantly. Similarly,

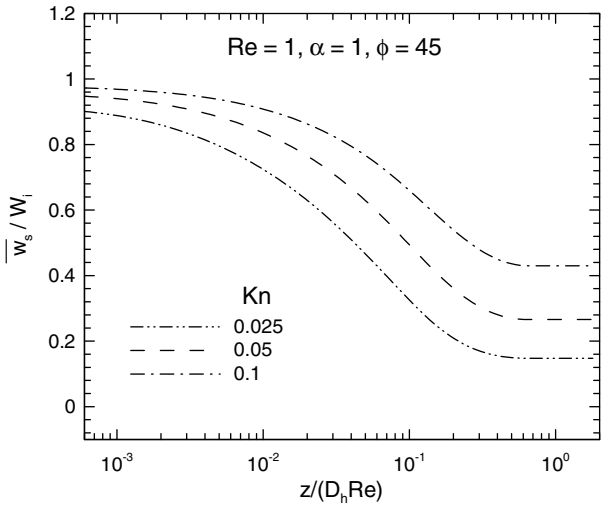

Fig. 5. Axial variation of velocity-slip as a function of *Kn* in a trapezoidal channel with $\phi = 45°$ and $\alpha = 1$ at $Re = 1$.

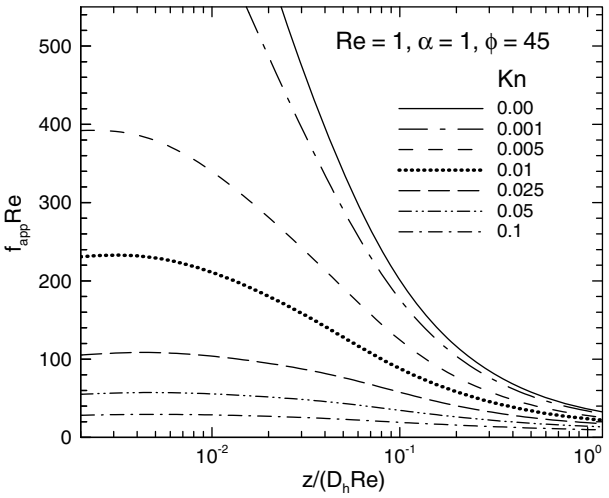

Fig. 6. Axial variation of apparent friction factor as a function of *Kn* in a trapezoidal channel with $\phi = 45°$ and $\alpha = 1$ at $Re = 1$.

much less pressure drop occurs due to lower wall shear as compared to no-slip conditions. Fig. 6 clearly shows that even small amounts of velocity-slip results in a very large reduction in the friction coefficient in the entrance region. Fig. 6 also indicates the existence of finite asymptotic values for the friction coefficient at the channel inlet. This is in contrast to no-slip flows, where $z^+ = 0$ is mathematically a plane of infinitely large wall shear. The observed asymptotic values of the friction coefficient as $z^+ \to 0$ can be estimated simply by combining Eq. (4) with the definition of the friction coefficient $\tau_w/(\rho W_i^2/2)$ to obtain [10]:

$$fRe \to (2/Kn)(\sigma_v/(2-\sigma_v)) \tag{8}$$

(note that there is a typographical error in [10]). In arriving at this equation, it has been assumed that $w_s \cong W_i$ in the immediate vicinity of the entrance. As shown in Fig. 5, this is a realistic assumption for $Kn \to 0.1$. Interestingly, this asymptotic limit is universal and is valid for any geometry because it is evaluated at a location where fluid is about to enter the channel, and therefore, there is no recognition of the geometry yet. Present numerical results, which include effects due to momentum flow rate changes, agree reasonably well with the estimated asymptotic values at higher Knudsen numbers as $z^+ \to 0$.

Geometric effects on the friction coefficient are studied by variation of aspect ratios and side angles in Fig. 7 for channel flows at $Re = 1$. Fig. 7a shows the fully developed values of the friction factor as a function of *Kn* for channels with different aspect ratios and a fixed side angle of $\phi = 45°$. For $Kn = 0$, the values of *fRe* compare well with the results of Shah and London [25] at all aspect ratios. As expected, *fRe* decreases monotonically with increasing *Kn*, which is about 45% of the no-slip case at $Kn = 0.1$ for an aspect ratio of $\alpha = 2$, while this value increases to about 50% of the no-slip case for an aspect ratio of $\alpha = 0.25$ at the same *Kn*. Similar behavior is observed for other side angles as well.

Fully developed values of the friction factor as a function of *Kn* for channels with different side angles and a fixed aspect ratio of $\alpha = 1$ are shown in Fig. 7b for $Re = 1$. Again the no-slip values of the friction coefficient compare well with the results of Shah and London [25] at all side angles. Furthermore, there is a comparison in this figure with the results of Morini et al. [9], who have performed an analysis of fully developed flows for a wide range of aspect ratios and Knudsen numbers. However, only a single side angle of $\phi = 54.74°$ (corresponding to microchannels fabricated by etching a silicon substrate) was considered. Fig. 7b shows that the friction coefficients decrease dramatically with increasing *Kn*

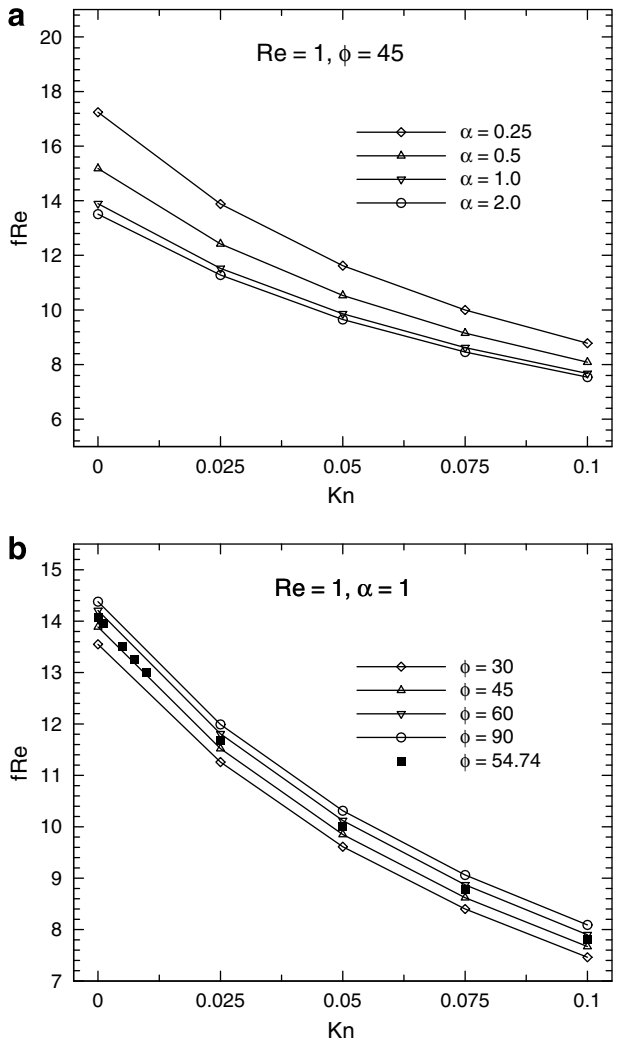

Fig. 7. Variation of fully developed values of *fRe* as a function of *Kn* for flow at *Re* = 1: (a) different channel aspect ratios and fixed side angle $\phi = 45^\circ$ and (b) different channel side angles and fixed aspect ratio $\alpha = 1$.

for all side angles to about 55% of their no-slip values at *Kn* = 0.1. Fig. 7b also shows that the friction coefficients decrease slightly as the side angle is reduced such that a trapezoidal channel with $\phi = 30^\circ$ has about 8% lower *fRe* than a square duct. The trends in this figure are consistent with the fact that velocity gradients become increasingly weaker in the corner regions with decreasing side angle. Finally, a comparison of Fig. 7a with Fig. 7b indicates clearly that the friction coefficient has a much stronger sensitivity to aspect ratio than side angle for trapezoidal microchannels.

4.2. The temperature field

The temperature fields in both the entrance and fully developed regions are strongly affected by both velocity-slip and temperature-jump at the walls, which create opposing effects on heat transfer. Velocity-slip by itself is expected to increase heat transfer rates since it enhances advection near the walls. On the other hand, heat transfer rates are adversely influenced by temperature-jump at the wall, which produces a thermal contact resistance effect. Fig. 8 shows the isotherms at *Re* = 10 in a trapezoidal microchannel with $\phi = 45^\circ$ and $\alpha = 1$ at the same three axial locations as in Fig. 3. In this figure, the solid lines are for the case of *Kn* = 0.1 while the dashed lines refer to no-slip/jump conditions with *Kn* = 0. Allowing for temperature-jump causes the fluid temperature adjacent to the

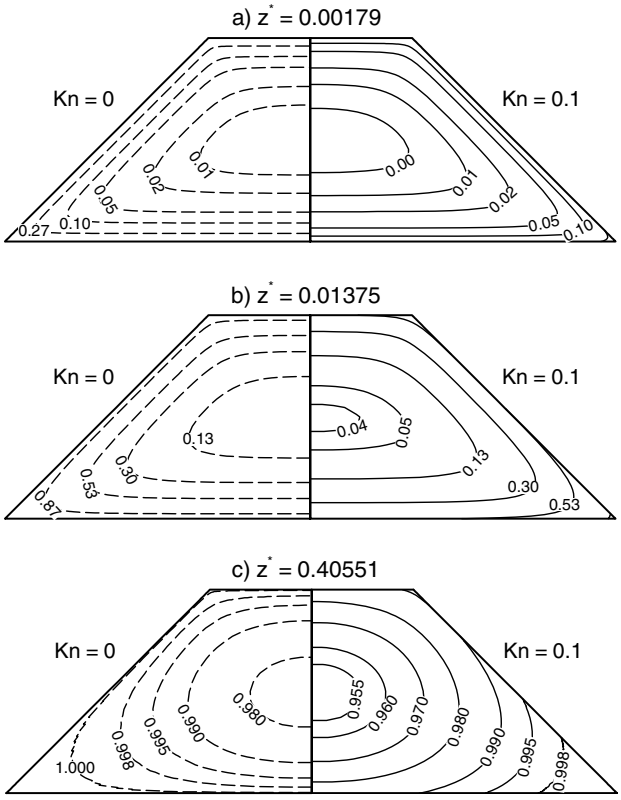

Fig. 8. Cross-sectional temperature distributions at *Re* = 10, $\phi = 45^\circ$, and $\alpha = 1$: dashed lines *Kn* = 0, solid lines *Kn* = 0.1; (a) $z^* = 0.00179$, (b) $z^* = 0.01375$ and (c) $z^* = 0.40551$.

wall to vary peripherally as seen in Fig. 8b, and with more clarity in the fully developed region in Fig. 8c. As expected, temperature-jump at the wall reduces the heat transfer rates, and thus, leads to lower fluid temperatures at the same axial location along the channel.

It is also useful to study the peripherally averaged temperature-jump along the channel, which is shown in Fig. 9 for a channel with $\phi = 45^\circ$ and $\alpha = 1$ at *Re* = 1. Similar to velocity-slip, temperature-jump is also very large near the channel inlet, which increases with *Kn*. Farther downstream, temperature-jump approaches zero for all

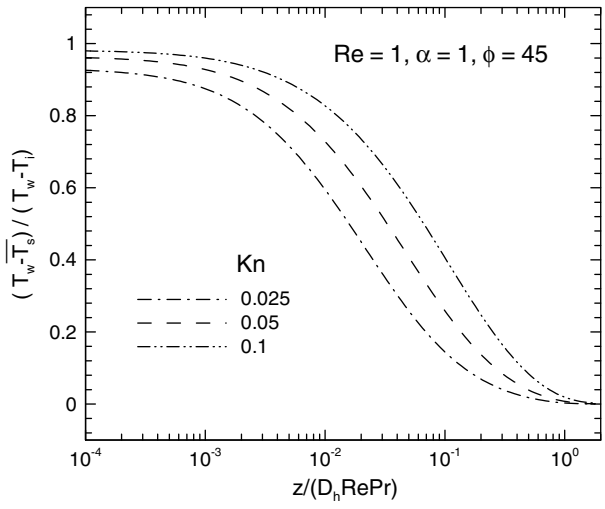

Fig. 9. Axial variation of temperature-jump as a function of *Kn* in a trapezoidal channel with $\phi = 45^\circ$ and $\alpha = 1$ at *Re* = 1.

Knudsen numbers as the fluid temperature reaches the wall temperature, and hence, all temperature gradients vanish.

The variations in the heat transfer coefficient along the main flow direction for a channel with $\phi = 45^\circ$ and $\alpha = 1$ at several Knudsen numbers are shown in Fig. 10 for $Re = 1$. The peripherally-averaged heat transfer coefficient or the Nusselt number is defined as:

$$Nu = \frac{hD_h}{k} = \frac{D_h(\overline{\partial T/\partial n})_w}{T_m - T_w} \tag{9}$$

where $\overline{(\partial T/\partial n)}_w$ is the peripherally-averaged temperature gradient normal to the wall at a given axial location, and T_m is the bulk mean temperature defined as:

$$T_m = \frac{1}{A_c W_i}\int_{A_c} T\vec{V}\cdot\vec{n}\,dA_c \tag{10}$$

In the present work, $Pr = 1$ in all cases considered, and therefore, the nondimensional axial position $z^* = z/(D_h RePr)$ or the reciprocal Graetz number is the same as z^+.

As mentioned before, velocity-slip by itself would increase heat transfer; however, the reduction due to temperature-jump outweighs this increase such that the net effect is a decrease in the heat transfer rate. As shown in Fig. 10, the reduction is very large early in the entrance region, which is consistent with the earlier observations associated with Fig. 9. Fig. 10 also indicates the existence of finite asymptotic values for Nu as $z^+ \to 0$ for slip-flows, which can be easily estimated by inserting the temperature-jump condition (Eq. 5) into the definition of Nusselt number (Eq. 9), resulting in:

$$Nu \to [((2-\sigma_T)/\sigma_T)(2\gamma/(\gamma+1))(Kn/Pr)]^{-1} \tag{11}$$

In arriving at this equation, it has been assumed that $T_m \cong T_s$ in the immediate vicinity of the entrance, which is a realistic assumption for larger Kn. Similar to the Poiseuille number asymptote discussed earlier, the Nu asymptote is also independent of Re and geometry since it is evaluated at a position where the flow has no recognition of the geometry, and therefore, of the Reynolds number. This can be clearly seen by comparing Figs. 10, 11 where the axial variations of Nu are shown for a channel with $\phi = 30^\circ$ and $\alpha = 1$ at the same Knudsen numbers but for $Re = 10$. Although geometry and Re have changed, the inlet values are identical and compare well with the corresponding estimates from Eq. (11). As expected, the accuracy of the asymptotic predictions using this equation deteriorates as $Kn \to 0$.

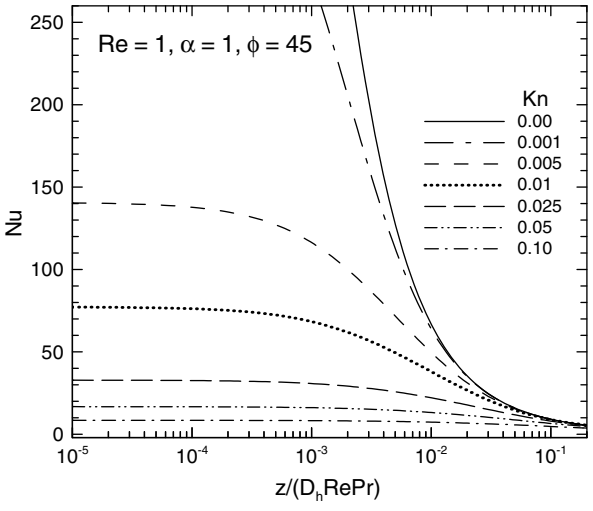

Fig. 10. Axial variation of Nusselt number as a function of Kn in a trapezoidal channel with $\phi = 45^\circ$ and $\alpha = 1$ at $Re = 1$.

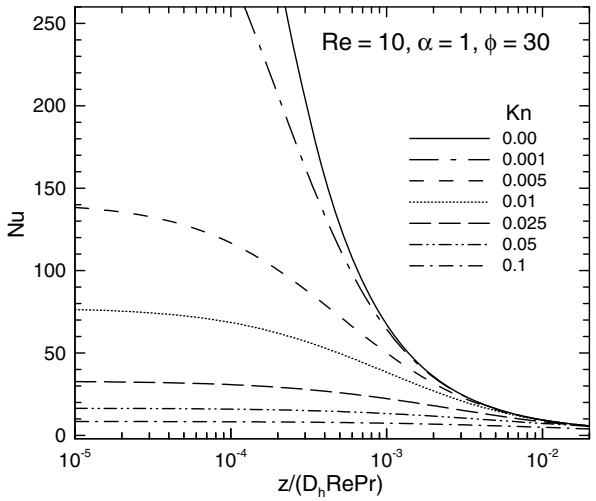

Fig. 11. Axial variation of Nusselt number as a function of Kn in a trapezoidal channel with $\phi = 30^\circ$ and $\alpha = 1$ at $Re = 10$.

Despite the dramatic reduction in heat transfer rates that occur with any level of rarefaction effects, the values of Nu in the entrance region are still much larger than those in the fully developed region. This highlights the importance of the entrance region in determining the heat transfer characteristics of short microchannels found in some micro devices. Due to the existence of large axial gradients close to the inlet, the effects of Re cannot be ignored. This is especially true at low Reynolds numbers typical of micro flows.

The effects of channel geometry on the heat transfer rates are studied by varying side angles and aspect ratios at $Re = 1$ in Fig. 12. Fig. 12a shows the variations of the fully developed heat transfer coefficients as a function of Kn for different aspect ratios, while the side angle is held constant at $\phi = 45^\circ$. It is observed that, as the aspect ratio decreases and the trapezoidal cross-section approaches the parallel-plates limit, the heat transfer rates increase. For larger aspect ratios, the cross-section tends towards a triangular one with lower Nu. Fig. 12a also indicates a stronger Nu dependence on the Kn as the aspect ratio decrease. For example, there is a 30% decrease in Nu at $Kn = 0.1$ for $\alpha = 0.25$ as compared to the no-slip case, while the reduction is about 15% for $\alpha = 2$. This effect can be explained considering the fact that as the aspect ratio decreases, the corner regions lose their influence, and therefore, the slip/jump effects become more uniform peripherally. On the other hand, at high aspect ratios, there is a strong non-uniformity around the channel periphery with the corner regions behaving closer to the no-slip/jump conditions, and therefore, the overall sensitivity to rarefaction is weaker. These observations are consistent with earlier findings [10] that flow in a square channel shows less sensitivity to rarefaction effects than flow between parallel plates.

Variations of fully developed Nu as a function of Kn and side angle are shown in Fig. 12b for a fixed aspect ratio of $\alpha = 1$. This figure confirms a monotonic reduction in Nu with increasing Kn for all side angles. The heat transfer rates are also found to decrease significantly with decreasing side angle, such that at $\phi = 30^\circ$ and $\alpha = 1$, the Nusselt numbers are lower by about 25% for all Kn as compared to a square duct. This can be explained by the fact that, for a fixed aspect ratio, the region of weak advection in the acute corners expands as ϕ decreases, resulting in a reduction of the overall heat transfer rate for that cross-section.

For convenience and future comparisons, the fully developed values of the friction and heat transfer coefficients as a function of Knudsen number are presented in Table 1 for different Reynolds numbers, side angles and aspect ratios.

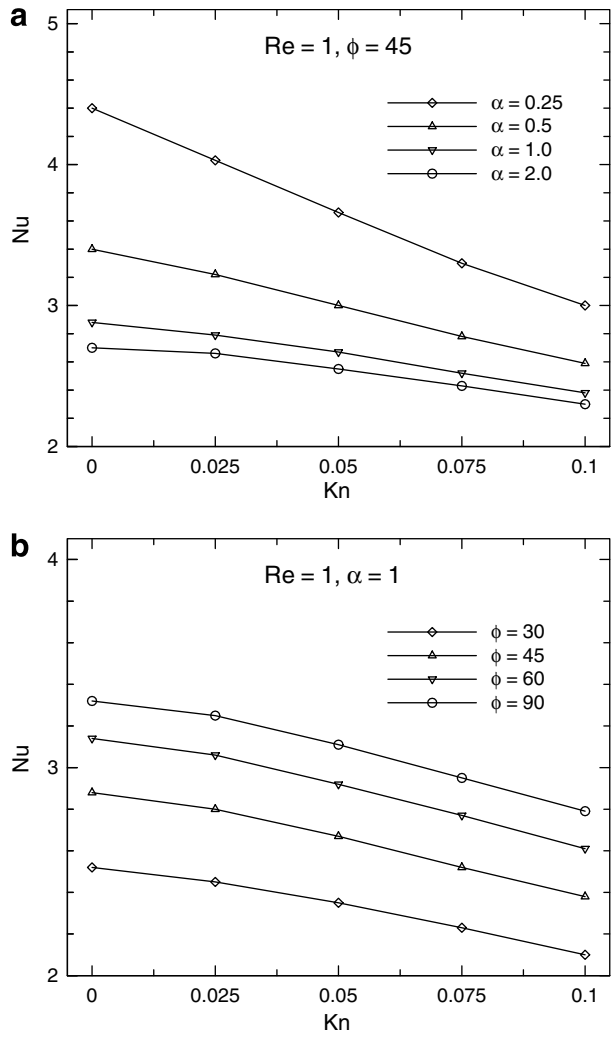

Fig. 12. Variation of fully developed Nu as a function of Kn at $Re = 1$: (a) different aspect ratios with $\phi = 45°$ and (b) different side angles with $\alpha = 1$.

5. Correlations

Friction factor and Nusselt number correlations previously developed by Renksizbulut and Niazmand [24] for no-slip-flows in rectangular and trapezoidal channels were further modified [10] for rarefaction effects as given below:

$$(fRe)_{fd} = \left[13.9(90^\circ/\phi)^{-0.07} + 10.4\exp\left(-3.25\alpha(90^\circ/\phi)^{0.23}\right)\right]G_1 \quad (12\text{-a})$$

$$G_1 = 1 - 2.48Kn^{0.64}(1 - 0.2\tanh(3\alpha)) \quad (12\text{-b})$$

$$(Nu)_{fd} = \left[2.87(90^\circ/\phi)^{-0.26} + 4.8\exp\left(-3.9\alpha(90^\circ/\phi)^{0.21}\right)\right]G_2G_3 \quad (13\text{-a})$$

$$G_2 = 1 - 1.75Kn^{0.64}(1 - 0.72\tanh(2\alpha)) \quad (13\text{-b})$$

$$G_3 = 1 + 0.075(1+\alpha)\exp(-0.45RePr) \quad (13\text{-c})$$

The rarefaction effects are introduced into the friction coefficients of rectangular and trapezoidal channels by the term G_1 given in Eq. (12-a). In the absence of any rarefaction effect, $G_1 = 1$ and Eq. (12-b) predicts the available data for a wide range of aspect ratios with a high level of accuracy (within 3%) [24]. When rarefaction effects are considered, Eq. (12) predicts the data for rectangular microchannels within 5% and trapezoidal microchannels within 6% as shown in Fig. 13. In this figure, the numerical results of Morini et al. [9] for slip-flow in rectangular and trapezoidal ($\phi = 54.74°$) microchannels with different aspect ratios are also included.

Eq. (13) predicts the present numerical heat transfer coefficients for all aspect ratios and side angles studied here within 10% as shown in Fig. 14. The rarefaction effects are introduced by G_2, while G_3 represents the Reynolds number dependence which is more pronounced at low Pe where axial conduction in the fluid cannot be ignored. Pahor and Strnad [26] studied the relative importance of axial conduction for flow between parallel plates and found a contribution of about 10% increase in heat transfer rates in the limit of vanishing Pe. Clearly, gas flows in microchannels are typically low Peclet number flows, and this correction is important. Considerable data is provided in [10] for rectangular microchannels with a wide range of aspect ratios, which are also predicted by Eq. (13) within 7% and plotted in Fig. 14.

Table 1
Poiseuille (fRe) and Nusselt (Nu) numbers for fully developed flow in trapezoidal channels

$Re = 0.1$								
Kn	$\alpha = 1, \phi = 30°$		$\alpha = 1, \phi = 45°$		$\alpha = 1, \phi = 60°$		$\alpha = 1, \phi = 90°$	
	$(fRe)_{fd}$	$(Nu)_{fd}$	$(fRe)_{fd}$	$(Nu)_{fd}$	$(fRe)_{fd}$	$(Nu)_{fd}$	$(fRe)_{fd}$	$(Nu)_{fd}$
0.000	13.35	2.64	13.88	2.91	14.09	3.22	14.33	3.45
0.025	10.98	2.59	11.51	2.88	11.81	3.18	11.95	3.41
0.050	9.55	2.54	9.75	2.79	10.15	3.03	10.26	3.34
0.100	7.38	2.37	7.59	2.63	7.89	2.75	8.07	3.18
$Re = 1$								
Kn	$\alpha = 0.25, \phi = 45°$		$\alpha = 0.25, \phi = 60°$		$\alpha = 0.5, \phi = 45°$		$\alpha = 0.5, \phi = 60°$	
	$(fRe)_{fd}$	$(Nu)_{fd}$	$(fRe)_{fd}$	$(Nu)_{fd}$	$(fRe)_{fd}$	$(Nu)_{fd}$	$(fRe)_{fd}$	$(Nu)_{fd}$
0.000	17.24	4.38	18.03	4.67	15.18	3.30	15.65	3.67
0.025	13.88	4.03	14.40	4.36	12.42	3.22	12.80	3.48
0.050	11.62	3.66	12.03	3.99	10.53	3.02	10.85	3.25
0.100	8.82	3.06	9.07	3.22	8.09	2.59	8.34	2.80
Kn	$\alpha = 0.5, \phi = 90°$		$\alpha = 1, \phi = 30°$		$\alpha = 1, \phi = 45°$		$\alpha = 1, \phi = 60°$	
	$(fRe)_{fd}$	$(Nu)_{fd}$	$(fRe)_{fd}$	$(Nu)_{fd}$	$(fRe)_{fd}$	$(Nu)_{fd}$	$(fRe)_{fd}$	$(Nu)_{fd}$
0.000	15.50	3.69	13.35	2.53	13.88	2.88	14.09	3.14
0.025	12.75	3.58	10.98	2.44	11.51	2.79	11.81	3.06
0.050	10.86	3.44	9.55	2.37	9.75	2.67	10.15	2.92
0.100	8.41	3.19	7.38	2.10	7.59	2.38	7.89	2.60
Kn	$\alpha = 1, \phi = 90°$		$\alpha = 2, \phi = 45°$		$\alpha = 2, \phi = 60°$			
	$(fRe)_{fd}$	$(Nu)_{fd}$	$(fRe)_{fd}$	$(Nu)_{fd}$	$(fRe)_{fd}$	$(Nu)_{fd}$		
0.000	14.33	3.32	13.51	2.70	13.97	3.03		
0.025	11.95	3.27	10.95	2.65	11.65	2.97		
0.050	10.26	3.20	9.65	2.55	9.99	2.84		
0.100	8.07	2.75	7.54	2.31	7.82	2.56		
$Re = 10$								
Kn	$\alpha = 0.5, \phi = 60°$		$\alpha = 0.5, \phi = 90°$		$\alpha = 1, \phi = 30°$		$\alpha = 1, \phi = 45°$	
	$(fRe)_{fd}$	$(Nu)_{fd}$	$(fRe)_{fd}$	$(Nu)_{fd}$	$(fRe)_{fd}$	$(Nu)_{fd}$	$(fRe)_{fd}$	$(Nu)_{fd}$
0.000	15.65	3.36	15.50	3.43	13.35	2.23	13.88	2.60
0.025	12.80	3.19	12.75	3.28	10.98	2.18	11.51	2.55
0.050	10.85	3.00	10.86	3.11	9.55	2.11	9.75	2.40
0.100	8.34	2.62	8.41	2.81	7.38	1.87	7.59	2.20
Kn	$\alpha = 1, \phi = 60°$		$\alpha = 1, \phi = 90°$		$\alpha = 2, \phi = 60°$			
	$(fRe)_{fd}$	$(Nu)_{fd}$	$(fRe)_{fd}$	$(Nu)_{fd}$	$(fRe)_{fd}$	$(Nu)_{fd}$		
0.000	14.09	2.83	14.33	3.05	13.97	2.77		
0.025	11.81	2.82	11.95	2.98	11.65	2.72		
0.050	10.15	2.68	10.26	2.88	9.99	2.61		
0.100	7.89	2.42	8.07	2.67	7.82	2.38		

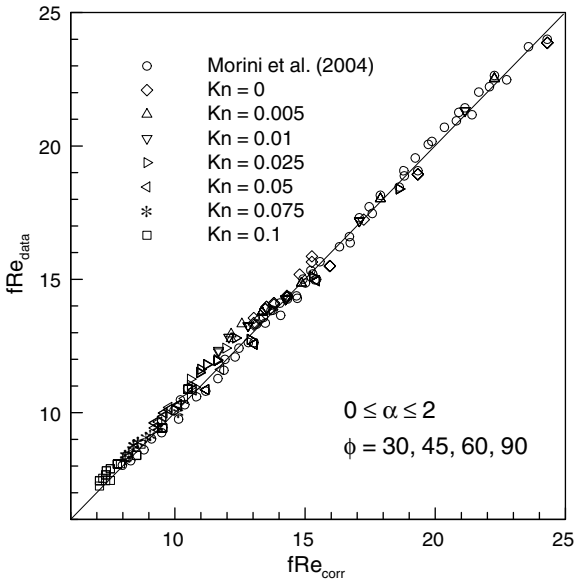

Fig. 13. Comparison of available data with the friction coefficient correlation (Eq. 12).

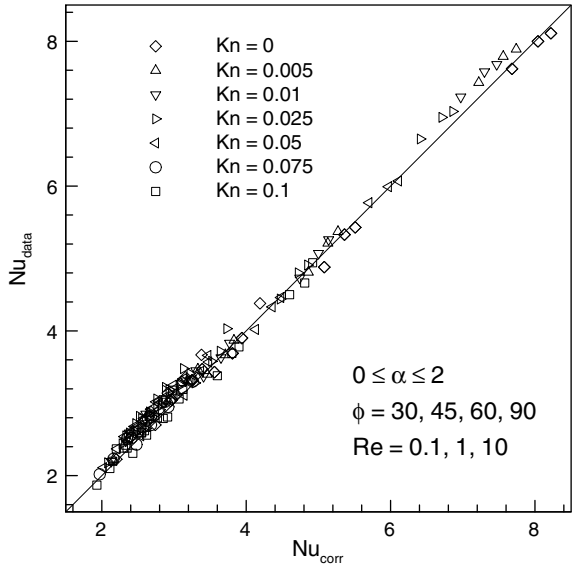

Fig. 14. Comparison of available data with the heat transfer correlation (Eq. 13).

It is also important to note that the friction and heat transfer coefficients for trapezoidal channels are quite sensitive to certain side angles at higher aspect ratios. Results by Shah and London [25] show that both coefficients undergo significant non-monotonic variations in the side angle range $75° \leqslant \phi \leqslant 85°$ if $\alpha > 2$, in which case the correlations given above lose their accuracy.

6. Conclusions

A control-volume based numerical method has been employed to examine gas rarefaction effects in simultaneously developing 3D laminar flows in trapezoidal microchannels with constant wall temperatures and *Re* in the range $0.1 \leqslant Re \leqslant 10$ with $Pr = 1$ for $Kn \leqslant 0.1$. The flow and heat transfer characteristics in the slip-flow regime were analyzed for different channel aspect ratios ($0.25 \leqslant \alpha \leqslant 2$) and side angles ($\phi = 30°, 45°, 60°, 90°$). An important feature of flow development from a prescribed uniform inlet velocity profile is the emergence of velocity over-shoots such that maximum axial velocities appear near the walls and especially at the corners regions as opposed to the channel core. This effect is more pronounced in the continuum regime ($Kn < 0.001$) with the no-slip boundary condition; yet still present to a lower extent even at higher Knudsen numbers.

In the slip-flow regime, the momentum and heat transfer rates are very significantly reduced in the entrance region due to high levels of velocity-slip and temperature-jump at the walls. An interesting feature associated with the slip-flow regime is the existence of asymptotic inlet values for both the Poiseuille and Nusselt numbers. These asymptotic values are directly related to the Knudsen number, but independent of the channel geometry and Reynolds number.

In the fully developed region, the momentum and heat transfer rates are again significantly affected by the degree of rarefaction, aspect ratio and side angle. Both the friction and heat coefficients monotonically decrease with increasing *Kn* and aspect ratio, and decreasing side angles. The friction coefficient shows the strongest dependence on rarefaction effects and weakest dependence on the channel side angle. The heat transfer coefficient shows less sensitivity to rarefaction effects with increasing channel aspect ratio. Practical engineering correlations are also provided for Poiseuille and Nusselt numbers associated with rectangular and trapezoidal microchannels.

Acknowledgement

Financial support of the Natural Sciences and Engineering Research Council of Canada is greatly appreciated.

References

[1] E.M. Sparrow, T.S. Lundgren, S.H. Lin, Slip flow in the entrance region of a parallel plate channel, Proceedings of the Heat transfer and Fluid Mechanics Institute, Stanford University Press, 1962 (pp. 223–38).
[2] R.W. Hanks, Velocity profile development in the entrance region of a tube and a parallel plate channel, Phys. Fluids 6 (11) (1963) 1645–1648.
[3] C.D. Meinhart, S.T. Wereley, J.G. Santiago, PIV measurements of a microchannel flow, Exp. Fluids 27 (1999) 414–419.
[4] S.E. Turner, L.C. Lam, M. Faghri, O.J. Gregory, Experimental investigation of gas flow in microchannels, J. Heat Transfer 126 (2004) 753–763.
[5] J.C. Harley, Y. Huand, H. Bau, J.N. Zemel, Gas flow in microchannels, J. Fluid Mech. 284 (1995) 257–274.
[6] E.B. Arkilic, M.A. Schmidt, K.S. Breuer, Gaseous slip-flow in long microchannels, J. Microelectromech. Syst. 6 (2) (1997) 167–178.
[7] A. Beskok, G.E. Karniadakis, A model for flows in channels pipes and ducts at micro and nano scales, Microscale Thermophys. Eng. 3 (1999) 43–77.
[8] J. Jang, S.T. Wereley, Pressure distribution of gaseous slip-flow in straight and uniform rectangular microchannels, Microfluidics Nanofluidics 1 (2004) 41–51.
[9] G.L. Morini, M. Spiga, P. Tartarini, The rarefaction effects on the friction factor of gas flow in microchannels, Superlattices Microstruct. 35 (2004) 587–599.
[10] M. Renksizbulut, H. Niazmand, G. Tercan, Slip-flow heat transfer in rectangular microchannels with constant wall temperature, Int. J. Therm. Sci. 45 (2006) 870–881.
[11] B. Cao, G.W. Chen, Q. Yuan, Fully developed laminar flow and heat transfer in smooth trapezoidal microchannel, Int. Commun. Heat Mass Transfer 32 (2005) 1211–1220.
[12] F.E. Larrodé, C. Housiadas, Y. Drossinos, Slip-flow heat transfer in circular tubes, Int. J. Heat Mass Transfer 43 (2000) 2669–2680.
[13] S. Yu, T.A. Ameel, Slip-flow heat transfer in rectangular microchannels, Int. J. Heat Mass Transfer 44 (2001) 4225–4234.
[14] S. Yu, T.A. Ameel, Slip-flow convection in isoflux rectangular microchannels, J. Heat Transfer 124 (2002) 346–355.
[15] P. Lee, S.V. Garimella, Thermally developing flow and heat transfer in rectangular microchannels of different aspect ratios, Int. J. Heat Mass Transfer 49 (2006) 3060–3067.
[16] C-E. Zhen, Z-C. Hong, Y-J. Lin, N-T. Hong, Comparison of 3D 2D DSMC heat transfer calculations of low speed short microchannel flows, Numer. Heat Transfer A 52 (2007) 239–250.

[17] C. Hong, Y. Asako, Heat transfer characteristics of gaseous flows in a microchannel and a microtube with constant wall temperature, Numer. Heat Transfer A 52 (2007) 219–238.
[18] G. Hetsroni, A. Mosyak, E. Pogrebnyak, L.P. Yarin, Heat transfer in microchannels: comparison of experiments with theory and numerical results, Int. J. Heat Mass Transfer 48 (2005) 5580–5601.
[19] G. Maranzana, I. Perry, D. Maillet, Mini- and micro-channels: influence of axial conduction in the walls, Int. J. Heat Mass Transfer 47 (2004) 3994–4004.
[20] E.H. Kennard, Kinetic Theory of Gases, McGraw-Hill, New York, 1939.
[21] L.B. Wigton, N.J. Yu, D.P. Young, GMRES acceleration of computational fluid dynamics codes, AIAA Computational Fluid Dynamics Meeting, Cinn., Ohio, 1985. pp. 67–74.
[22] A.J. Chorin, Numerical solution of the Navier–Stokes equations, Math. Comput. 22 (1968) 745–762.
[23] H.A. Dwyer, Calculation of droplet dynamics in high temperature environments, Prog. Energy Combust. Sci. 15 (1989) 131–158.
[24] M. Renksizbulut, H. Niazmand, Laminar flow and heat transfer in the entrance region of trapezoidal channels with constant wall temperature, J. Heat Transfer 128 (2006) 63–74.
[25] R.K. Shah, A.L. London, Laminar flow forced convection in ducts, Advances in Heat Transfer, Academic Press, New York, 1978.
[26] S. Pahor, J. Strnad, A note on heat transfer in laminar flow through a gap, Appl. Sci. Res. Sect. A 10 (1961) 81–84.